Nanoscale

Accepted Manuscript

This article can be cited before page numbers have been issued, to do this please use: K. Hayashi, R. Kishida and K. Ishikawa, *Nanoscale*, 2026, DOI: 10.1039/D6NR01077F.

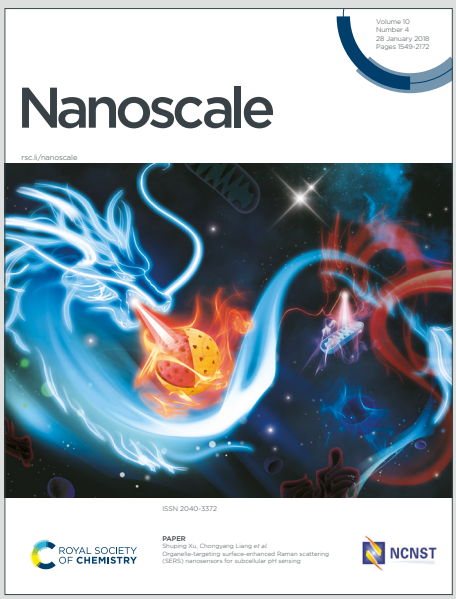

ROYAL SOCIETY OF CHEMISTRY

rsc.li/nanoscale

View Article Online
DOI: 10.1039/D6NR01077F

Multiscale Porous Carbonate Apatite Honeycomb Granules Derived from a Metastable Calcium Carbonate Precursor for Enhanced Bone Formation

Koichiro Hayashi,* Ryo Kishida, and Kunio Ishikawa

Department of Biomaterials, Faculty of Dental Science, Kyushu University
3-1-1 Maidashi, Higashi-ku, Fukuoka 812-8582, Japan
Phone: +81-82-642-6345
E-mail: khayashi@dent.kyushu-u.ac.jp

*Corresponding author

Keywords: apatite; calcium carbonates; honeycomb; metastable phase; bone; granules

Abstract

Global population aging has increased the clinical demand for maintaining and restoring skeletal function. The bone regenerative capacity of synthetic bone substitutes is strongly influenced by pore architecture. Although well-controlled large-pore structures have been widely reported, the precise regulation of pore structures at the submicron and nanoscale remains challenging. In this study, we developed a strategy to control the multiscale pore characteristics of a material by exploiting the differences in the properties of vaterite and calcite, which are metastable and stable calcium carbonate precursors, respectively. To isolate the effect of submicron and nanoporous structures, carbonate apatite (CA) honeycomb (HC) granules with identical chemical compositions and channel architectures but different submicron and nanoporous structures were fabricated. HC green bodies composed of vaterite or calcite powders were produced by extrusion molding, followed by debinding and phosphate treatment to convert them into CA through a dissolution–precipitation reaction. Both the vaterite-derived (V-CA-HC) and calcite-derived (C-CA-HC) HC granules consisted of AB-type CA containing approximately 9% carbonate and exhibited the same HC channel size (110 μm) and wall thickness (120 μm). However, the submicron and nanoporous structures of the two types of HC granules differed significantly. The V-CA-HC granules exhibited bimodal pore structures with modal diameters of 14 and 336 nm, whereas the C-CA-HC granules exhibited a unimodal distribution centered at 41 nm. In a rabbit femoral condyle critical-size defect model, V-CA-HC granules induced

View Article Online
DOI: 10.1039/D6NR01077F

significantly greater new bone formation than C-CA-HC granules at both 4 and 12 weeks post-implantation. These results demonstrate that submicron and nanoporous structures independently regulate bone formation when the macroporous structure is kept constant, and that submicron and nanoporous structures provide a versatile strategy for designing multiscale porous bone substitutes.

1. Introduction

Globally, populations are aging, and the widening gap between healthy life expectancy and average life expectancy has become a significant societal challenge.[1-4] Extending healthy life expectancy requires the maintenance and restoration of musculoskeletal function, with bone health playing a particularly critical role.[5-11] With the age-related rise in falls, tumors, osteoarthritis, and dental implant treatments, artificial bone substitutes are used in diverse clinical settings, including the repair of fractures and bone defects.[12-19] Bone injuries and defects also occur in young populations owing to various causes, such as trauma and disease, and thus the demand for synthetic bone substitutes is high.[20, 21]

Autologous bone grafting remains the gold standard for bone regeneration, reconstruction, and augmentation. However, autologous bone grafting has several limitations, including high invasiveness and the limited volume of harvestable bone.[22] Allogeneic and xenogeneic bone grafts are also applied in certain cases, but concerns remain regarding immune rejection and infection risk.[22, 23] Although synthetic bone substitutes have been used clinically for decades because they avoid these issues, their bone-forming and bone-substituting capacities still fall short of those of autologous bone.[22] Consequently, the enhancement of the bone-forming and bone-substituting functions of synthetic bone substitutes is required for their application in critical-sized bone defects.

One key factor influencing the bone-forming ability and bioresorbability of a synthetic bone substitute is its material composition. Synthetic bone substitutes include calcium phosphate-based materials, such as hydroxyapatite (HA) and beta-tricalcium phosphate.[24-26] Carbonate apatite (CA), also a synthetic bone substitute, whose inorganic composition closely resembles that of native bone, gradually resorbs following bone formation and is ultimately replaced by newly formed bone. However, bone formation and material resorption are not solely determined by composition; rather, bone regeneration properties are strongly influenced by the pore structure of the material. [27, 28]

The pore structures of synthetic bone substitutes can be broadly classified into large (>100 μm) and small pores (<10 μm), with each pore structure playing a distinct role. Large pore structures influence the ingrowth of tissues, such as bone, blood vessels, and fibrous tissue, into the material. In general, pore sizes ranging from 100 to 600 μm are considered suitable for bone and vascular

View Article Online
DOI: 10.1039/D6NR01077F

formation.[27, 29] Furthermore, bone formation is reported to be favored when pore sizes are 300 μm or smaller while fibrous tissue ingrowth becomes dominant when pore sizes exceed 400 μm.[30] In addition to pore size, pore interconnectivity is also critical because interconnected channels enable cell infiltration, angiogenesis, and nutrient and waste product diffusion, ultimately promoting bone formation.[27, 31, 32]

Submicron- and nanoscale porous structures increase the specific surface area and surface roughness of synthetic bone substitutes, thereby enhancing the adsorption of proteins, such as bone morphogenetic proteins and collagen.[33-39] The enhanced protein adsorption promotes cell adhesion, osteogenic differentiation, and apatite deposition, ultimately leading to new bone formation.[33-39] In addition to the presence of submicron pores and nanopores, their volume and size distribution also play critical roles. Increased submicron pore volumes and pore volumes smaller than 100 nm promote osteoclast formation and regulates the resorption behavior of the material, which in turn influences the bone formation process.[34, 36-39] Pores smaller than 1 μm can be broadly classified into submicron pores (100 nm to 1 μm) and nanopores (<100 nm), with each class contributing differently to bone regeneration. Submicron pores effectively promote bone formation, whereas nanopores strongly influence osteoclast formation and accelerate material resorption.[36, 38, 39] Therefore, precise control of pore size distribution in the submicron and nanometer ranges is essential for regulating the initial biological responses to the material, the duration of its scaffolding function, and its resorption behavior.

Taken together, large pores and submicron/nanoporous structures play distinct and complementary roles, and neither alone is sufficient for optimal bone regeneration. Therefore, synthetic bone substitutes are required to possess a multiscale porous structure incorporating both large pores and submicron/nanoporous structures. [38, 40-45] To date, synthetic bone substitutes with multiscale porosity have been fabricated using three-dimensional (3D) printing or adaptive foam reticulation combined with subsequent debinding and sintering in which slurries composed of ceramic powders mixed with polymer microspheres or oil droplets are used.[44, 46-48] In these approaches, large pores are formed by 3D printing or adaptive foam reticulation, while submicron and nanoporous structures are generated by removing porogens such as polymer microspheres or oil droplets. Although 3D printing offers the advantage of designed large pore architectures, its fabrication accuracy becomes insufficient when pore sizes are below 300 μm.[44, 46, 47] Adaptive foam reticulation produces irregular large pore structures, making the precise control of pore size and morphology difficult.[48] Furthermore, when a porogen is used to create submicron and nanopores, the pore size is determined by the porogen diameter.[44, 48] In conventional porogen-based fabrication methods for ceramic bone substitutes, the pore size is often determined by the diameter of sacrificial templates such as polymer microspheres or oil droplets, which typically range from several to tens of micrometers.[44, 48]

View Article Online
DOI: 10.1039/D6NR01077F

Therefore, the formation of submicron pores and nanopores remains challenging in these systems. Similarly, when oil droplets are used, the diameters of the resulting submicron and nanopores depend on droplet size and typically range from several to tens of micrometers, which also hinders the formation of submicron pores and nanopores.[46, 47]

Given the aforementioned background, this study aimed to fabricate CA honeycomb (HC) granules (CA-HC granules) possessing a multiscale porous structure composed of highly interconnected HC-type large pores (that is, channels) with uniform size, submicron pores, and nanopores. Accordingly, the following approach was adopted. First, an HC-type large pore structure was fabricated by extrusion molding, which enabled the formation of interconnected channels with high dimensional accuracy.[49, 50] Secondly, to generate submicron pores and nanopores, vaterite, a metastable phase of calcium carbonate synthesized at a low temperature and characterized by a small crystal size and low density (2.55 g/cm^3), was used as a precursor of CA, resulting in the formation of abundant nano-to submicrometer-scale intercrystalline spaces—submicron pores and nanopores—in CA-HC granules.[51] For comparison purposes, CA-HC granules with no submicron pores and exhibiting a small submicron/nanopore volume were prepared using the precursor calcite, a thermodynamically stable calcium carbonate phase synthesized at a high temperature and characterized by a larger crystal size and higher density (2.71 g/cm^3) compared with the CA precursor.[51] Subsequently, the in vivo bone-forming ability and material resorption behavior of the CA-HC granules derived from vaterite (V-CA-HC granules) and calcite (C-CA-HC granules) were evaluated.

2. Materials and Methods

2.1. Fabrication of Honeycomb Green Bodies (HC-GBs)

Using extrusion molding, we previously fabricated HC green bodies (HC-GBs) composed of various calcium-based powders and organic binders.[49, 50] In this study, we prepared HC-GBs using calcium hydroxide powder (Nacalai Tesque, Kyoto, Japan) and a wax-based organic binder (Nagamine wax binder, Nagamine Manufacturing, Nakatado, Japan) via a method similar to that reported previously. Calcium hydroxide powder with an average particle size of 1 μm, obtained by jet milling, was mixed with the organic binder at a volume ratio of 1:1. The mixture was kneaded at 150 °C for 2 h using a roller mixer installed in a kneading and extrusion apparatus (Labo Plastomill, Toyoseiki Co., Toyo, Japan). The resulting kneaded compound was then loaded into a single-screw extruder (Labo Plastomill) equipped with an HC extrusion die featuring a slit width of 150 μm and pitch of 300 μm (Nagamine Manufacturing). HC-GB blocks were subsequently fabricated by extrusion molding (Figure 1A).

View Article Online
DOI: 10.1039/D6NR01077F

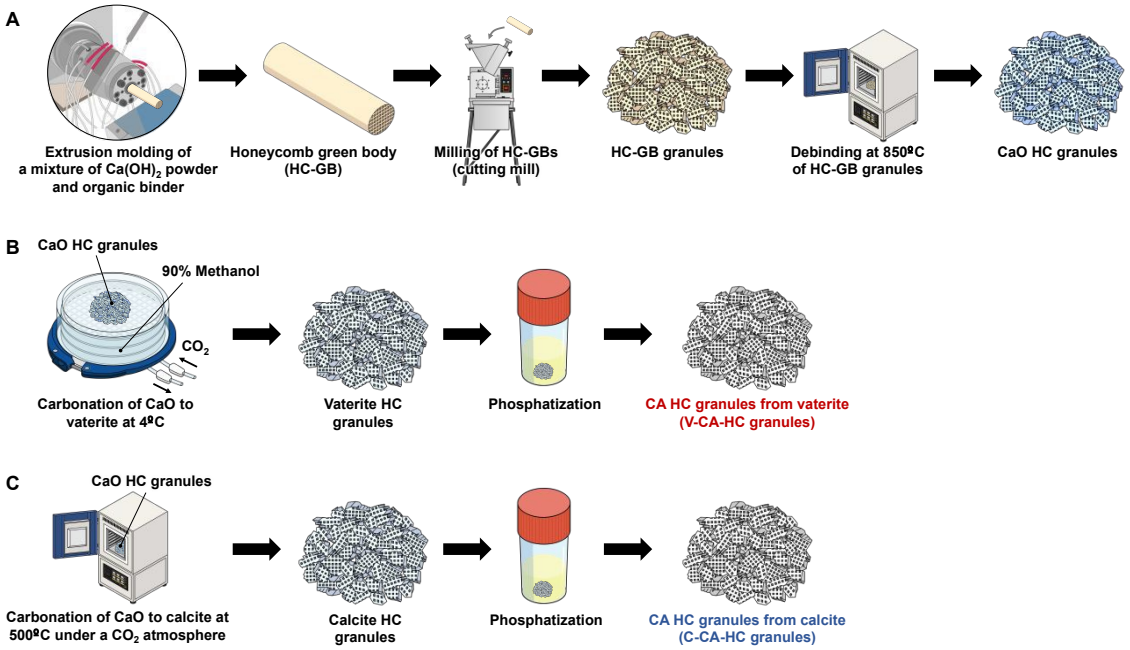

Figure 1. Schematic of the fabrication processes for carbonate apatite (CA) honeycomb (HC) granules derived from vaterite (V-CA-HC granules) and calcite (C-CA-HC granules). (A) Extrusion molding of HC green bodies and their granulation using a cutting mill, followed by debinding and sintering to obtain CaO HC granules. (B) Fabrication of vaterite HC granules through compositional conversion of CaO HC granules to vaterite, followed by phosphatization to convert vaterite into CA, yielding V-CA-HC granules. (C) Fabrication of calcite HC granules through compositional conversion of CaO HC granules to calcite, followed by phosphatization to convert calcite into CA, yielding C-CA-HC granules.

2.2. Fabrication of CaO Honeycomb Granules

HC-GB blocks were crushed into granules using a cutting mill (Figure 1A). The obtained HC-GB granules were subsequently heat-treated in an electric furnace (Nitto Kagaku Co., Ltd., Nagoya, Japan). The furnace temperature was increased to 850 ℃ at a heating rate of approximately 0.1 ℃/min under an ambient air atmosphere, followed by sintering at 850 ℃ for 3 h to obtain CaO HC granules.

2.3. Fabrication of V-CA-HC Granules

Vaterite HC granules were fabricated by converting CaO into vaterite using a modified method based on the method reported by Kathyola et al.[52] The CaO HC granules were immersed in 90% methanol (FUJIFILM Wako Pure Chemical Corporation, Osaka, Japan) while carbon dioxide was continuously bubbled at a flow rate of 200 mL/min. A reaction was conducted at 4 ℃ for 5 d to induce compositional conversion from CaO to vaterite (Figure 1B). The resulting vaterite HC granules were subsequently phosphate treated by immersion in a 1 mol/L aqueous Na_2HPO_4 solution (FUJIFILM

View Article Online
DOI: 10.1039/D6NR01077F

Wako Pure Chemical Corporation) at 80 ℃ for 7 d, yielding V-CA-HC granules. Finally, the obtained V-CA-HC granules were thoroughly washed multiple times with distilled water.

2.4. Fabrication of C-CA-HC Granules

Calcite HC granules were obtained by heat treating CaO HC granules at 500 ℃ for 5 d under a CO_2 atmosphere (Figure 1C). The resulting calcite HC granules were subsequently phosphate-treated by immersion in a 1 mol/L aqueous Na_2HPO_4 solution (FUJIFILM Wako Pure Chemical Corporation) at 80 ℃ for 7 d, yielding C-CA-HC granules. Finally, the obtained C-CA-HC granules were thoroughly washed multiple times with distilled water.

2.5. Material Characterization

The crystalline phases of the test samples were identified by X-ray diffraction (XRD) using a diffractometer (D8 Advance, Bruker AXS GmbH, Karlsruhe, Germany) with Cu Kα radiation. The accelerating voltage and current were set to 40 kV and 40 mA, respectively. The functional groups of the samples were analyzed by Fourier transform infrared spectroscopy (FTIR) using an FTIR spectrometer (FT/IR-6200, JASCO, Tokyo, Japan) with the KBr disk method. The carbonate contents of the samples were quantified using a CHN coder (MT-6, Yanako Analytical Instruments, Kyoto, Japan). The microstructures of the samples were observed using scanning electron microscopy (SEM, S-3400N, Hitachi High-Technologies, Tokyo, Japan) at an accelerating voltage of 15 kV. Prior to the SEM observations, the samples were coated with an Au–Pd layer using a magnetron sputtering system (MSP-1S, Vacuum Device Co., Ibaraki, Japan). The particle sizes of the HC granules were determined by measuring the Feret diameters of 300 randomly selected particles. The channel diameter and wall thickness were measured from 50 randomly selected channels and pore walls in the SEM images using ImageJ software. The pore size distribution and pore volume of the samples were evaluated using mercury intrusion porosimetry (MIP, AutoPore 9420, Shimadzu, Kyoto, Japan).

2.6. Ethical Statement

All animal experimental protocols were reviewed and approved by the Animal Experiment Committee of Kyushu University (Approval No. A30-237-0; Approval date: August 1, 2018).

2.7. Animal Experiments

Twelve 18-week-old male Japanese white rabbits (Japan SLC, Hamamatsu, Japan) were used in this study. The animals were first sedated by intramuscularly administering a mixture of ketamine (30 mg/kg, Ketalar®, Daiichi Sankyo Co., Ltd., Tokyo, Japan) and xylazine (5 mg/kg, Selactar®, Elanco, Indiana, USA). An auricular vein was then cannulated, and the rabbits were anesthetized by intravenously administering ketamine (10 mg/kg) and xylazine (3 mg/kg).

View Article Online
DOI: 10.1039/D6NR01077F

After shaving the area around the distal femur, the surgical site was disinfected by applying povidone-iodine. Local anesthesia was achieved by injecting 2% lidocaine at multiple sites surrounding the implantation area. A longitudinal skin incision of approximately 3 cm was made using a scalpel, and the bone surface was exposed by blunt dissection.

Critical-size bone defects, with a diameter of 6 mm and a depth of 4 mm, were created in the medial condyles of both distal femoral epiphyses using a trephine bur. [49, 53] This defect model is widely used for evaluating the bone regenerative capacity of biomaterials because spontaneous bone regeneration is limited during the experimental period.[49, 53] In our previous study using the same defect model, the defects were predominantly filled with adipose tissue rather than bone tissue.[49] Following defect creation, the defect sites were thoroughly irrigated with a saline solution. The V-CA-HC and C-CA-HC granules, which had been sterilized by dry heat at 170 ℃ for 3 h, were implanted into the femoral bone defects of the contralateral legs of the rabbits.

Following material implantation, the periosteum and skin of each rabbit were sutured using nylon monofilament sutures, and the surgical site was disinfected with povidone-iodine. Immediately after surgery and once daily for three consecutive days postoperatively, the animals received intramuscular injections of the antibiotic gentamicin (4 mg/kg, Gentacin®, Takata Pharmaceutical Co., Ltd., Saitama, Japan) and the analgesic buprenorphine hydrochloride (0.03 mg/kg, Lepetan®, Otsuka Pharmaceutical Co., Ltd., Tokyo, Japan).

2.8. Histological Analysis

At 4 and 12 weeks post-implantation of the materials into femoral bone defects, the rabbits were euthanized via an anesthesia overdose containing a mixture of ketamine and xylazine. The distal femoral epiphyses containing the implanted materials and surrounding tissues were removed en bloc and fixed by immersion in a solution of 10% neutral buffered formalin. Following fixation, the samples were decalcified using ethylenediaminetetraacetic acid disodium salt. The decalcified tissues were then dehydrated, cleared, and embedded in paraffin according to standard histological procedures. Sections with a thickness of 3 μm were prepared using a microtome. After deparaffinization, the prepared sections were stained with hematoxylin and eosin (H&E) using a conventional protocol.

2.9. Statistical Analysis

All quantitative data used in the study are presented as the mean ± standard deviation. Statistical analysis was performed using Student's t-test, and differences were considered statistically significant at $p < 0.05$.

3. Results

3.1. Material characterizations

View Article Online
DOI: 10.1039/D6NR01077F

The XRD patterns of vaterite and calcite HC granules revealed that their crystalline phases were vaterite and calcite, respectively (Figure 2A).[54] The XRD patterns of both V-CA-HC and C-CA-HC granules were consistent with those of apatitic crystals.[55] The FTIR spectra of V-CA-HC and C-CA-HC granules exhibited characteristic absorption bands at 1040, 960, 606, and 567 cm^{-1} attributed to PO_4^{3-}, similar to those observed in the spectrum of the reference material HA (Figure 2B).[56-58] Although an absorption band attributed to OH^- was observed at 629 cm^{-1} in the HA spectrum, this band was not observed in the spectrum of either V-CA-HC or C-CA-HC granules.[56-58] In addition, the absorption bands at 1475, 1417, and 870 cm^{-1} attributed to CO_3^{2-} were observed in the spectra of V-CA-HC and C-CA-HC granules, whereas no such bands were detected in the HA spectrum.[56-58] The CO_3^{2-}-related absorption bands at 1475 and 1417 cm^{-1} indicated the substitution of OH^- and PO_4^{3-} sites by CO_3^{2-}, respectively.[56-58] CHN analysis showed that the carbonate contents of V-CA-HC and C-CA-HC granules were 9.2 ± 3.5 wt% and 9.4 ± 3.7 wt%, respectively, with no significant difference between the two groups (Figure 2C).

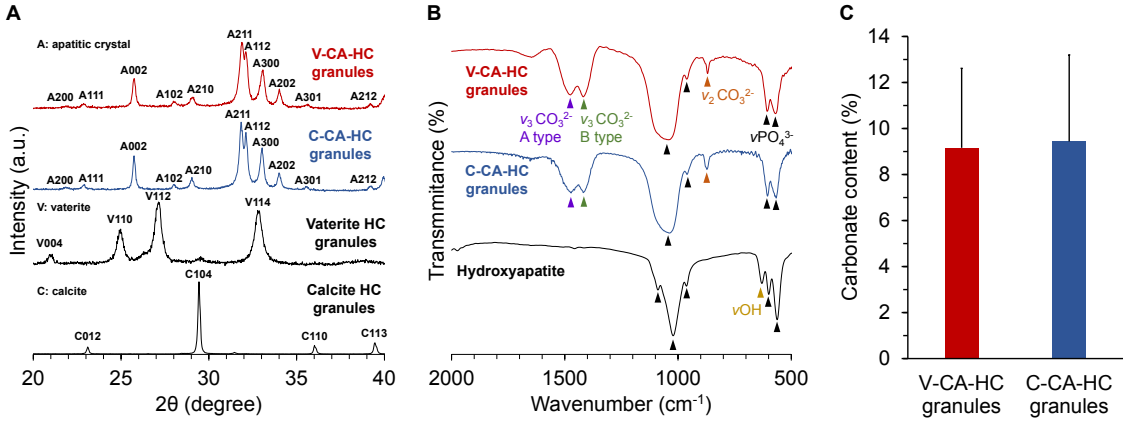

Figure 2. (A) X-ray diffraction patterns of vaterite and calcite honeycomb (HC) and carbonate apatite (CA) HC granules derived from vaterite (V-CA-HC granules) and calcite (C-CA-HC granules). (B) Fourier transform infrared spectra of V-CA-HC granules, C-CA-HC granules, and the reference material hydroxyapatite. Black, orange, green, purple, and yellow arrowheads indicate absorption bands attributed to νPO_4^{3-}, νCO_3^{2-}, νCO_3^{2-} B-type substitution (replacement of PO_4^{3-} by CO_3^{2-}), νCO_3^{2-} A-type substitution (replacement of OH^- by CO_3^{2-}), and νOH^-, respectively. (C) Carbonate contents of V-CA-HC and C-CA-HC granules measured by CHN analysis.

SEM observations showed that the vaterite HC granules were composed of spherical particles (Figure S1A), whereas the calcite HC granules consisted of aggregates of smaller, irregularly shaped particles (Figure S1B). The particle sizes of the vaterite and calcite granules were 1.4 ± 0.6 μm and 0.7 ± 0.3 μm, respectively (Figure S1C). Numerous uniaxial channels penetrated the V-CA-HC granules (Figure 3A). The channels were separated by walls and regularly arranged, exhibiting a uniform channel size and wall thickness (Figures 3A and 3B). The channel walls were composed of

View Article Online
DOI: 10.1039/D6NR01077F

spherical aggregates consisting of CA crystals (Figure 3C). Similarly, the C-CA-HC granules also exhibited a large number of regularly arranged uniaxial channels, and the channel walls were composed of spherical aggregates of CA crystals (Figures 3D–F). However, the spherical aggregates constituting the C-CA-HC granules were larger than those observed in the V-CA-HC granules (Figures 3C and 3F). The edge lengths of the square channels in the V-CA-HC and C-CA-HC granules were 109.9 ± 6.7 and 109.7 ± 4.9 μm, respectively (Figure 3G). The wall thicknesses of the V-CA-HC and C-CA-HC granules were 119.8 ± 8.0 μm and 119.9 ± 6.7 μm, respectively (Figure 3H). Thus, both the channel size and wall thickness were nearly identical between the V-CA-HC and C-CA-HC granules. In contrast, the diameter of the spherical aggregates in the V-CA-HC granules was 0.8 ± 0.1 μm, which was less than half of that observed in the C-CA-HC granules at 2.0 ± 0.3 μm and a significant difference ($p = 2.0\times10^{-23}$) was detected between the two groups (Figure 3I).

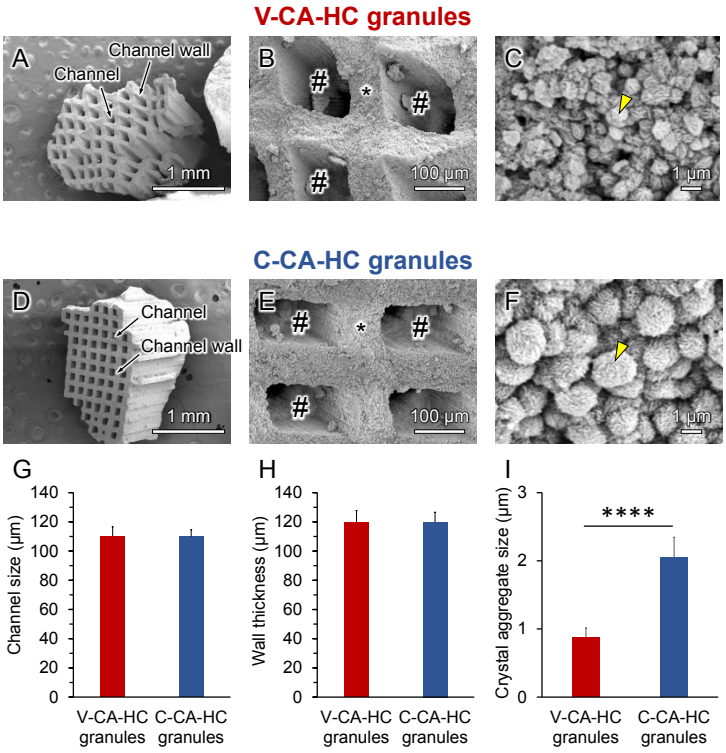

Figure 3. Scanning electron microscopy images of (A)–(C) V-CA-HC and (D)–(F) C-CA-HC granules. (B) and (E) show higher-magnification images corresponding to (A) and (D), respectively. (C) and (F) show higher-magnification images corresponding to (B) and (E), respectively. Symbols #, *, and yellow arrowheads indicate the channels, channel walls, and spherical aggregates of CA crystals, respectively. (G) Channel size, (H) channel wall thickness, and (I) diameter of the spherical aggregates of CA crystals. Data are shown as the mean ± standard deviation. Statistical analysis was performed using Student's t-test at $^{****}p < 0.001$.

MIP revealed that both V-CA-HC and C-CA-HC granules exhibited a prominent peak at

View Article Online
DOI: 10.1039/D6NR01077F

approximately 100 μm in their pore size distribution profiles, corresponding to channels (Figure 4A). The peaks observed at pore sizes larger than 200 μm were attributed to intergranular spaces. The V-CA-HC granules exhibited a bimodal pore size distribution with two distinct modal pore diameters of 14 and 336 nm. In contrast, the C-CA-HC granules exhibited a unimodal pore size distribution with a single modal pore diameter of 41 nm. Cumulative pore volume analysis demonstrated that although the channel volumes of the V-CA-HC and C-CA-HC granules were comparable, the submicron and nanopore volume of the V-CA-HC granules was markedly greater than that of the C-CA-HC granules (Figure 4B). The quantitative evaluation of channel volumes showed that both V-CA-HC and C-CA-HC granules exhibited identical channel volumes of 0.11 cm^3/g. The V-CA-HC and C-CA-HC granules exhibited submicron pore volumes of 0.18 and 0.01 cm^3/g and nanopore volumes of 0.20 and 0.08 cm^3/g, respectively, resulting in a total submicron and nanopore volume of V-CA-HC granules that was more than four times greater than that of C-CA-HC granules (Figure 4C).

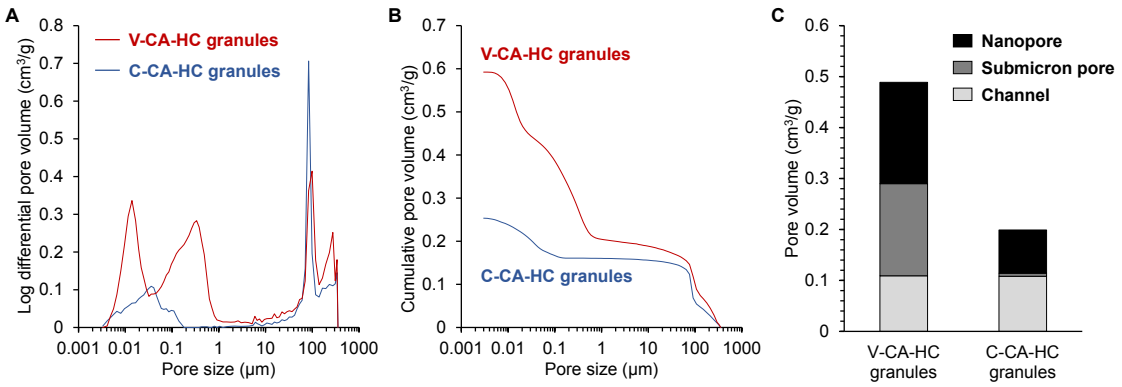

Figure 4. Mercury intrusion porosimetry results of V-CA-HC and C-CA-HC granules. (A) Relationship between pore size and pore volume. (B) Relationship between pore size and cumulative pore volume. (C) Quantitative analysis of channel, submicron pore, and nanopore volumes.

3.2. In vivo evaluations

Histological analysis by H&E staining at 4 weeks after implantation into critical-sized femoral bone defects in rabbits demonstrated that both V-CA-HC and C-CA-HC granules induced new bone formation within and around the granules (Figures 5A–5F). However, a clear difference in the amount of newly formed bone was observed between the two groups. Marked differences were observed in bone formation in the intergranular spaces. Abundant bone tissue was formed among the V-CA-HC granules (Figure 5B), whereas areas occupied by tissues other than bone were observed among the C-CA-HC granules (Figure 5E). Differences were also evident in bone formation within the granules. In the V-CA-HC group, the channels were filled with newly formed bone (Figure 5C). By contrast, in the C-CA-HC group, bone formation was observed along the channel wall surfaces, and no bone formation was detected in the central regions of the channels (Figure 5F). Furthermore, in both V-CA-

View Article Online
DOI: 10.1039/D6NR01077F

HC and C-CA-HC groups, osteoclasts and osteoblasts were observed on the channel walls and newly formed bone surfaces, respectively (Figures 5C and 5F).

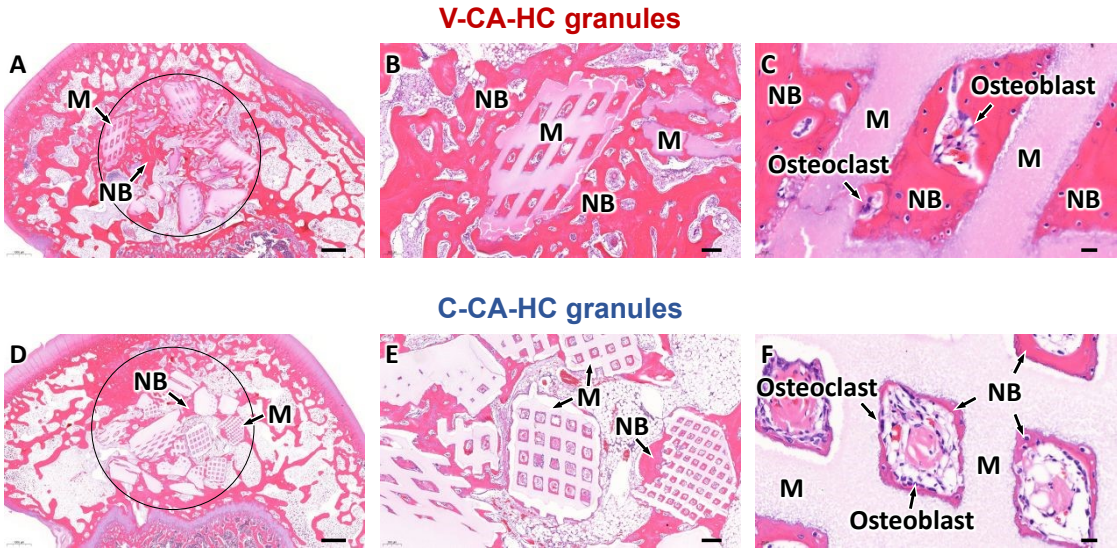

Figure 5. Histological analysis by hematoxylin and eosin staining at 4 weeks after implantation of (A)–(C) V-CA-HC and (D)–(F) C-CA-HC granules. (B) and (E) show higher-magnification images of the granules and surrounding tissues. (C) and (F) show higher-magnification images of the tissues formed within the channels of the granules. M, NB, and the black ring indicate the material, newly formed bone, and the boundary of the bone defect, respectively. Scale bars are as follows: (A) and (D) 1 mm, (B) and (E) 200 μm, and (C) and (F) 20 μm.

At 12 weeks after implantation, bone formation behavior similar to that observed at 4 weeks were also evident (Figures 6A–6F). The V-CA-HC granules exhibited greater bone formation than the C-CA-HC granules, both within the channels and in the intergranular spaces.

View Article Online
DOI: 10.1039/D6NR01077F

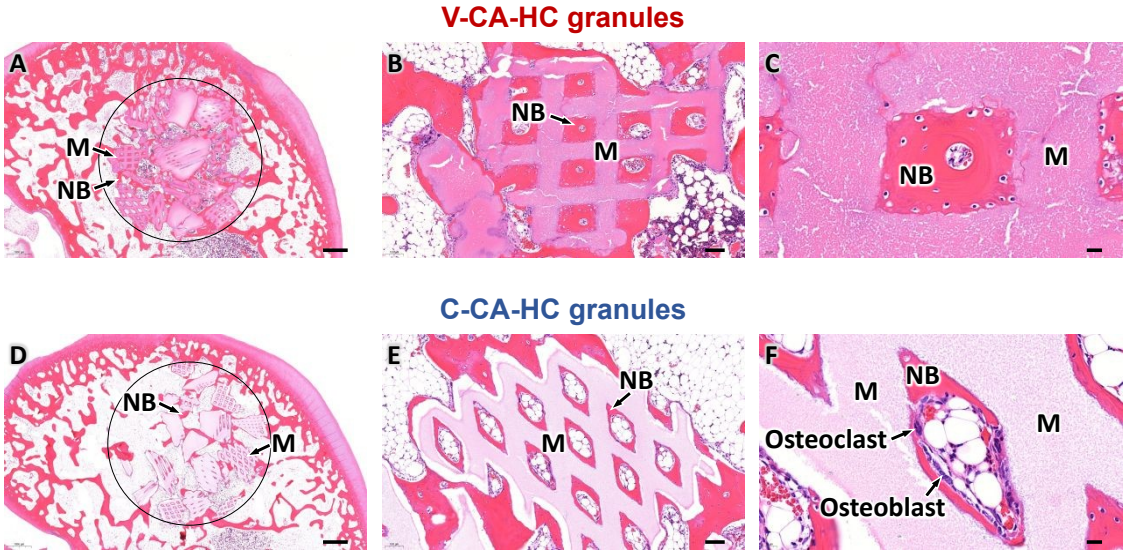

Figure 6. Histological analysis by hematoxylin and eosin staining at 12 weeks after implantation of (A)–(C) V-CA-HC and (D)–(F) C-CA-HC granules. (B) and (E) show higher-magnification images of the granules and surrounding tissues. (C) and (F) show higher-magnification images of the tissues formed within the channels of the granules. M, NB, and the black ring indicate the material, newly formed bone, and the boundary of the bone defect, respectively. Scale bars are as follows: (A) and (D) 1 mm, (B) and (E) 200 μm, and (C) and (F) 20 μm.

Quantitative histological analysis revealed that the proportion of newly formed bone within bone defects was significantly higher in the V-CA-HC group than in the C-CA-HC group at both 4 and 12 weeks after implantation (Figure 7A, $p = 0.002$ at 4 weeks and $p = 0.025$ at 12 weeks). In contrast, no significant difference in the proportion of residual material was observed between the V-CA-HC and C-CA-HC groups at 4 weeks. At 12 weeks, however, the proportion of the residual material in the V-CA-HC group was significantly lower than that in the C-CA-HC group (Figure 7B, $p = 0.029$).

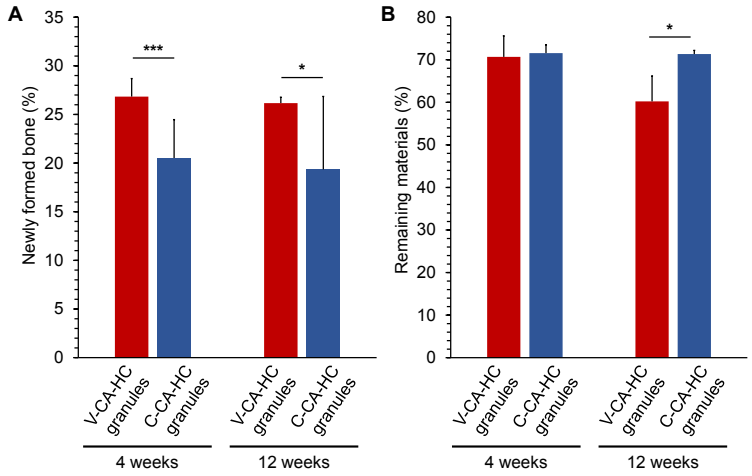

View Article Online
DOI: 10.1039/D6NR01077F

Figure 7. Quantitative histological analysis of (A) newly formed bone and (B) residual material within bone defects at 4 and 12 weeks after granule implantation. Data are shown as mean ± standard deviation (n = 6). Statistical analysis was performed using the Student's t-test at $*p < 0.05$ and $***p < 0.005$.

4. Discussion

V-CA-HC and C-CA-HC granules are both AB-type CA containing approximately 9% carbonate ions. The two types of granules share comparable macroscopic architectures, characterized by HC structures with similar channel sizes, channel wall thicknesses, and channel volumes. However, their submicron and nanoporous structures differ markedly. V-CA-HC granules exhibit a bimodal pore size distribution with modal diameters of 14 and 336 nm, whereas C-CA-HC granules display a unimodal pore size distribution with a single modal diameter of 41 nm. Hence, V-CA-HC granules contain both submicron pores and nanopores, whereas C-CA-HC granules contain markedly fewer submicron pores and predominantly consist of nanopores. Compared with the C-CA-HC granules, the V-CA-HC granules exhibited approximately 30-fold greater submicron pore volume, 2-fold greater nanopore volume, and 4-fold greater total pore volume below 1 μm. Furthermore, the V-CA-HC granules promote significantly greater early-stage new bone formation compared with the C-CA-HC granules. More importantly, because the macroscopic HC structures are essentially identical between the two materials, the observed differences in bone formation can be primarily attributed to the differences in the submicron and nanoporous structures rather than to channel-related effects.

The differences in the submicron and nanoporous structures between the V-CA-HC and C-CA-HC granules can be attributed to three factors: (1) differences in the morphology and size of the precursor vaterite and calcite particles, (2) differences in the dissolution behavior of the precursors and the subsequent nucleation and crystal-growth processes during conversion to CA, and (3) differences in the size of the resulting CA aggregates.

The difference in the submicron pore structures can be explained as follows. The particle sizes of the vaterite and calcite precursors were 1.4 ± 0.6 μm and 0.7 ± 0.3 μm, respectively. In contrast, the sizes of the CA aggregates in the final V-CA-HC and C-CA-HC granules were approximately 0.8 ± 0.1 μm and 2.0 ± 0.3 μm, respectively. Thus, the aggregate size decreased during the conversion from vaterite to CA, whereas it increased during the conversion from calcite to CA. This opposite particle-size evolution during the dissolution–precipitation conversion process likely influenced the interaggregate void structure. Specifically, the reduction in aggregate size in the V-CA-HC granules would increase the interstitial spaces between the aggregates, whereas the increase in aggregate size in the C-CA-HC granules would reduce such spaces. Furthermore, the smaller aggregates in the V-

View Article Online
DOI: 10.1039/D6NR01077F

CA-HC granules likely hindered dense packing because of increased interparticle interactions and bridging phenomena, thereby increasing the interaggregate void fraction and promoting the formation of interconnected submicron pores.[59, 60] Accordingly, submicron pores with a modal diameter of 336 nm observed in the V-CA-HC granules are considered to originate primarily from the interstitial spaces among the aggregates.

The difference in the nanoporous structures can be explained in a different manner. The nanopores observed in both materials are considered to originate mainly from intercrystalline spaces within the spherical CA aggregates. Because vaterite is more soluble than calcite,[61] the vaterite precursor likely dissolved more rapidly during phosphatization, resulting in the formation of a larger number of CA nuclei. Consequently, finer CA crystals were formed in the V-CA-HC granules, producing smaller intercrystalline spaces within the aggregates. In contrast, the slower dissolution of the calcite precursor likely resulted in fewer nuclei and greater crystal growth, leading to the formation of larger CA crystals and correspondingly larger intercrystalline spaces. As a result, smaller nanopores with a modal diameter of 14 nm were detected in the V-CA-HC granules, whereas larger nanopores with a modal diameter of 41 nm were detected in the C-CA-HC granules. These findings suggest that the nanopore size distribution reflects differences in the nucleation and crystal-growth behavior of CA arising from the distinct dissolution characteristics of the precursor phases.

Previous studies have reported that nanopores with sizes in the range of 10–30 nm increase the specific surface area, thereby enhancing protein adsorption, promoting cell adhesion, and inducing osteogenic differentiation, which ultimately contribute to enhanced bone formation.[43, 62] Kakuta et al. demonstrated that materials with a high abundance of submicron pores exhibited significantly increased numbers of tartrate-resistant acid phosphatase-positive cells (osteoclasts) together with enhanced new bone formation.[34] These results suggest that submicron pores and nanopores promote bone formation through different mechanisms. The abundance of both pore types in V-CA-HC granules likely accounts for their greater bone-forming ability compared with C-CA-HC granules.

In this study, we developed a strategy to control the submicron and nanopore characteristics of two materials with identical macroporous architectures by exploiting the differences in the properties of their calcium carbonate precursors. The strategy enabled the independent control of the pore structures of the materials across multiple length scales, including channels, submicron pores, and nanopores, an important design consideration for porous biomaterials. The strategy is versatile and can potentially be applied to various calcium phosphate materials with different macroporous architectures. Because it can be integrated with a wide range of material fabrication methods, the strategy would contribute to the development of diverse next-generation bone regenerative materials.

View Article Online
DOI: 10.1039/D6NR01077F

This study, however, has several limitations. In particular, parameters that could mediate the observed biological responses, such as protein adsorption and ion release kinetics, were not directly evaluated. Future studies will aim to quantitatively investigate these physicochemical interactions and clarify their relationship with the in vivo bone formation observed in the study.

Conclusion

In this study, CA-HC granules possessing identical macroporous structures but different submicron and nanoporous structures were successfully fabricated by exploiting the differences in the properties of metastable and stable calcium carbonate precursors. V-CA-HC granules exhibited a multiscale submicron and nanoporous structure composed of both nanopores and submicron pores, whereas C-CA-HC granules mainly contained nanopores with a smaller total submicron and nanopore volume. In a rabbit femoral condyle critical-size defect model, the V-CA-HC granules induced significantly greater bone formation than the C-CA-HC granules at both 4 and 12 weeks after implantation. Because the macroporous structures of the two materials were essentially identical, the results demonstrate that submicron and nanoporous structure plays a crucial role in regulating bone formation. The strategy enables independent control of macroporous, submicron, and nanoporous structures and provides a versatile approach for designing multiscale porous calcium phosphate-based materials for bone regeneration and other biomedical applications.

AUTHOR INFORMATION

Corresponding Author
Koichiro Hayashi
E-mail: khayashi@dent.kyushu-u.ac.jp

Author Contributions

Koichiro Hayashi: Conceptualization, Methodology, Investigation, Resources, Writing - Original Draft, Writing - Review & Editing, Supervision, Project administration, Funding acquisition.
Ryo Kishida: Investigation.
Kunio Ishikawa: Project administration

Funding Sources
This study was supported by the Japan Agency for Medical Research and Development (JP25ym0126811j0004), the Japan Society for the Promotion of Science (JP23K18593 and JP23K25208), and Japan Science and Technology Agency (JPMJTR25RJ and PRESTO JP25144773).

View Article Online
DOI: 10.1039/D6NR01077F

ACKNOWLEDGMENT

This research was supported by the Center for Clinical and Translational Research at Kyushu University.

References

[1] X. Cao, Y. Hou, X. Zhang, C. Xu, P. Jia, X. Sun, L. Sun, Y. Gao, H. Yang, Z. Cui, Y. Wang, Y. Wang, A comparative, correlate analysis and projection of global and regional life expectancy, healthy life expectancy, and their GAP: 1995-2025, J Glob Health 10(2) (2020) 020407.

[2] A. Garmany, A. Terzic, Global Healthspan-Lifespan Gaps Among 183 World Health Organization Member States, JAMA Netw Open 7(12) (2024) e2450241.

[3] A. Garmany, S. Yamada, A. Terzic, Longevity leap: mind the healthspan gap, NPJ Regen Med 6(1) (2021) 57.

[4] J.Y. Xi, J.G. Zhao, X.Q. Li, B. Yan, J.J. Bai, Y.N. Xiang, W. Hu, J. Hu, Y. Liao, J. Gu, X. Lin, Y.T. Hao, Quantifying the loss of healthy life expectancy due to population ageing: health benefit estimation from a global perspective, BMJ Glob Health 10(5) (2025).

[5] C. Chen, Y. Du, K. Cao, Y. You, L. Pi, D. Jiang, M. Yang, X. Wu, M. Chen, W. Zhou, J. Qi, D. Chen, R. Yan, C. Zhu, S. Yang, Global years lived with disability for musculoskeletal disorders in adults 70 Years and older from 1990 to 2019, and projections to 2040, Heliyon 10(15) (2024) e35026.

[6] S.Y. Guan, J.X. Zheng, X.Y. Feng, S.X. Zhang, S.Z. Xu, P. Wang, H.Y. Cai, H.F. Pan, The impact of population ageing on musculoskeletal disorders in 204 countries and territories, 1990-2021: global burden and healthcare costs, Ann Rheum Dis 84(12) (2025) 2128-2138.

[7] S.Y. Guan, J.X. Zheng, S.X. Zhang, S. Xu, Z. Shuai, H.Y. Cai, F. Pan, Global Burden of Musculoskeletal Disorders in Adults Aged 50 and Over, 1990-2021: Risk Factors and Sociodemographic Inequalities, J Cachexia Sarcopenia Muscle 16(4) (2025) e70008.

[8] R. Lewis, C.B. Gomez Alvarez, M. Rayman, S. Lanham-New, A. Woolf, A. Mobasheri, Strategies for optimising musculoskeletal health in the 21(st) century, BMC Musculoskelet Disord 20(1) (2019) 164.

[9] A. Nguyen, P. Lee, E.K. Rodriguez, K. Chahal, B.R. Freedman, A. Nazarian, Addressing the growing burden of musculoskeletal diseases in the ageing US population: challenges and innovations, Lancet Healthy Longev 6(5) (2025) 100707.

[10] J. Tan, Z. Zhu, X. Wang, B. Yang, S. Liu, M. Shi, Y. Luo, C. Du, Y. Sun, J. Liao, Y. Lei, W. Huang, Global burden and trends of musculoskeletal disorders in postmenopausal elderly women: a 1990-2021 analysis with projections to 2045, Arthritis Res Ther 27(1) (2025) 127.

View Article Online
DOI: 10.1039/D6NR01077F

[11] X. Yin, T. Deng, R. Ma, X. Fu, Y. Yin, X. Jia, F. Liu, Burden, trends, and predictions of five major musculoskeletal disorders in China, Japan, and South Korea: analysis based on the Global Burden of Disease Study 2021, Frontiers in Public Health 13 (2025).

[12] K. Chaabna, A. Jithesh, S. Khawaja, J. Aboughanem, R. Mamtani, S. Cheema, The epidemiology of unintentional falls among older people in the Middle East and North Africa: a systematic review and meta-analysis, J Glob Health 15 (2025) 04072.

[13] Y. Chen, Z. Wang, Z. Xu, L. Chen, Rising tides of knee osteoarthritis: global trends and regional disparities among middle-aged and elderly populations from 1990 to 2021 and its prediction to 2035, Frontiers in Musculoskeletal Disorders 3 (2025).

[14] G.B.D.O. Collaborators, Global, regional, and national burden of osteoarthritis, 1990-2020 and projections to 2050: a systematic analysis for the Global Burden of Disease Study 2021, Lancet Rheumatol 5(9) (2023) e508-e522.

[15] J. Ducommun, K. El Kholy, L. Rahman, M. Schimmel, V. Chappuis, D. Buser, Analysis of trends in implant therapy at a surgical specialty clinic: Patient pool, indications, surgical procedures, and rate of early failures-A 15-year retrospective analysis, Clin Oral Implants Res 30(11) (2019) 1097-1106.

[16] J. Lai, X. Li, W. Liu, Q. Liufu, C. Zhong, Global, regional, and national burden and trends analysis of malignant neoplasm of bone and articular cartilage from 1990 to 2021: A systematic analysis for the Global Burden of Disease Study 2021, Bone 188 (2024) 117212.

[17] Q. Xu, X. Ou, J. Li, The risk of falls among the aging population: A systematic review and meta-analysis, Front Public Health 10 (2022) 902599.

[18] B. Zhang, B. Dou, K. Li, Global, regional, and national burden of hip fractures attributable to falls in older adults: changes from 1990-2021 and 2036 projections, Front Public Health 13 (2025) 1674881.

[19] J. Zhou, B. Liu, M.Z. Qin, J.P. Liu, A prospective cohort study of the risk factors for new falls and fragility fractures in self-caring elderly patients aged 80 years and over, BMC Geriatr 21(1) (2021) 116.

[20] Y. Liu, L. He, L. Cheng, X. Li, M. Gao, Q. Li, J. Gao, M. Ramalingam, Enhancing Bone Grafting Outcomes: A Comprehensive Review of Antibacterial Artificial Composite Bone Scaffolds, Med Sci Monit 29 (2023) e939972.

[21] N. Xue, X. Ding, R. Huang, R. Jiang, H. Huang, X. Pan, W. Min, J. Chen, J.A. Duan, P. Liu, Y. Wang, Bone Tissue Engineering in the Treatment of Bone Defects, Pharmaceuticals (Basel) 15(7) (2022).

[22] M.P. Ferraz, Bone Grafts in Dental Medicine: An Overview of Autografts, Allografts and Synthetic Materials, Materials (Basel) 16(11) (2023).

[23] Z. Amini, R. Lari, A systematic review of decellularized allograft and xenograft-derived

View Article Online
DOI: 10.1039/D6NR01077F

513 scaffolds in bone tissue regeneration, Tissue Cell 69 (2021) 101494.
514 [24] P. Humbert, C. Kampleitner, J. De Lima, M.A. Brennan, I. Lodoso-Torrecilla, J.M. Sadowska,
515 F. Blanchard, C. Canal, M.P. Ginebra, O. Hoffmann, P. Layrolle, Phase composition of calcium
516 phosphate materials affects bone formation by modulating osteoclastogenesis, Acta Biomater 176
517 (2024) 417-431.
518 [25] P. Jin, L. Liu, L. Cheng, X. Chen, S. Xi, T. Jiang, Calcium-to-phosphorus releasing ratio
519 affects osteoinductivity and osteoconductivity of calcium phosphate bioceramics in bone tissue
520 engineering, Biomed Eng Online 22(1) (2023) 12.
521 [26] W. Lei, Y. Wu, H. Yuan, P. He, J. Wu, J. Chen, Y. Liu, H. Zhang, J.D. de Bruijn, X. Xiang, P.
522 Ji, H. Yuan, M. Li, Establishing rabbit critical-size bone defects to evaluate the bone-regeneration
523 potential of porous calcium phosphate ceramics, Front Bioeng Biotechnol 12 (2024) 1524133.
524 [27] M. Tavoni, M. Dapporto, A. Tampieri, S. Sprio, Bioactive Calcium Phosphate-Based
525 Composites for Bone Regeneration, Journal of Composites Science 5(9) (2021).
526 [28] H. Mohammadi, M. Sepantafar, N. Muhamad, A. Bakar Sulong, How Does Scaffold Porosity
527 Conduct Bone Tissue Regeneration?, Advanced Engineering Materials 23(10) (2021).
528 [29] E. Sadeghian Dehkord, B. De Carvalho, M. Ernst, A. Albert, F. Lambert, L. Geris, Influence
529 of physicochemical characteristics of calcium phosphate-based biomaterials in cranio-maxillofacial
530 bone regeneration. A systematic literature review and meta-analysis of preclinical models, Mater
531 Today Bio 26 (2024) 101100.
532 [30] K. Hayashi, M. Shimabukuro, R. Kishida, A. Tsuchiya, K. Ishikawa, Honeycomb scaffolds
533 capable of achieving barrier membrane-free guided bone regeneration, Materials Advances 2(23)
534 (2021) 7638-7649.
535 [31] F. He, T. Lu, X. Fang, S. Feng, S. Feng, Y. Tian, Y. Li, F. Zuo, X. Deng, J. Ye, Novel Extrusion-
536 Microdrilling Approach to Fabricate Calcium Phosphate-Based Bioceramic Scaffolds Enabling
537 Fast Bone Regeneration, ACS Appl Mater Interfaces 12(29) (2020) 32340-32351.
538 [32] G. Qian, T. Wu, J. Ye, Hierarchically porous calcium phosphate scaffold with degradable
539 PLGA microsphere network, Materials Chemistry and Physics 301 (2023).
540 [33] N. Abbasi, S. Hamlet, R.M. Love, N.-T. Nguyen, Porous scaffolds for bone regeneration,
541 Journal of Science: Advanced Materials and Devices 5(1) (2020) 1-9.
542 [34] A. Kakuta, T. Tanaka, M. Chazono, H. Komaki, S. Kitasato, N. Inagaki, S. Akiyama, K.
543 Marumo, Effects of micro-porosity and local BMP-2 administration on bioresorption of beta-TCP
544 and new bone formation, Biomater Res 23 (2019) 12.
545 [35] A.A. Vu, D.A. Burke, A. Bandyopadhyay, S. Bose, Effects of surface area and topography on
546 3D printed tricalcium phosphate scaffolds for bone grafting applications, Addit Manuf 39 (2021).
547 [36] K. Hayashi, K. Ishikawa, Effects of nanopores on the mechanical strength, osteoclastogenesis,
548 and osteogenesis in honeycomb scaffolds, J Mater Chem B 8(37) (2020) 8536-8545.

View Article Online
DOI: 10.1039/D6NR01077F

549 [37] K. Hayashi, R. Kishida, A. Tsuchiya, K. Ishikawa, Carbonate Apatite Micro-Honeycombed
550 Blocks Generate Bone Marrow-Like Tissues as well as Bone, Adv Biosyst 3(12) (2019) e1900140.
551 [38] K. Hayashi, A. Tsuchiya, M. Shimabukuro, K. Ishikawa, Multiscale porous scaffolds
552 constructed of carbonate apatite honeycomb granules for bone regeneration, Materials & Design
553 215 (2022).
554 [39] K. Hayashi, R. Kishida, K. Ishikawa, Effects of Micropore Size Distribution in Carbonate
555 Apatite Honeycomb Granules on Bone Replacement, J Biomed Mater Res A 114(2) (2026) e70033.
556 [40] J. Feng, J. Liu, Y. Wang, J. Diao, Y. Kuang, N. Zhao, Beta-TCP scaffolds with rationally
557 designed macro-micro hierarchical structure improved angio/osteo-genesis capability for bone
558 regeneration, J Mater Sci Mater Med 34(7) (2023) 36.
559 [41] M.N. Gomez-Cerezo, J. Pena, S. Ivanovski, D. Arcos, M. Vallet-Regi, C. Vaquette, Multiscale
560 porosity in mesoporous bioglass 3D-printed scaffolds for bone regeneration, Mater Sci Eng C
561 Mater Biol Appl 120 (2021) 111706.
562 [42] D. Jeyachandran, M. Cerruti, Glass, Ceramic, Polymeric, and Composite Scaffolds with
563 Multiscale Porosity for Bone Tissue Engineering, Advanced Engineering Materials 25(17) (2023).
564 [43] C. Kim, J.W. Lee, J.H. Heo, C. Park, D.H. Kim, G.S. Yi, H.C. Kang, H.S. Jung, H. Shin, J.H.
565 Lee, Natural bone-mimicking nanopore-incorporated hydroxyapatite scaffolds for enhanced bone
566 tissue regeneration, Biomater Res 26(1) (2022) 7.
567 [44] T. Lu, Y. Liang, L. Zhang, X. Yuan, J. Ye, Fabrication of β-TCP ceramic scaffold with
568 hierarchical pore structure using 3D printing and porogen: Investigation of osteoinductive and
569 bone defects repair properties, Applied Materials Today 40 (2024).
570 [45] H. Zhang, H. Zhang, Y. Xiong, L. Dong, X. Li, Development of hierarchical porous
571 bioceramic scaffolds with controlled micro/nano surface topography for accelerating bone
572 regeneration, Mater Sci Eng C Mater Biol Appl 130 (2021) 112437.
573 [46] S.S.L. Chan, J.R. Black, G.V. Franks, D.E. Heath, Hierarchically porous 3D-printed ceramic
574 scaffolds for bone tissue engineering, Biomater Adv 169 (2025) 214149.
575 [47] Q. Liu, T. Li, S.W. Gan, S.Y. Chang, C.C. Yen, W. Zhai, Controlling the hierarchical
576 microstructure of bioceramic scaffolds by 3D printing of emulsion inks, Additive Manufacturing
577 61 (2023).
578 [48] J. Winnett, N. Jumbu, S. Cox, G. Gibbons, L.M. Grover, J. Warnett, M.A. Williams, C.E.J.
579 Dancer, K.K. Mallick, In-vitro viability of bone scaffolds fabricated using the adaptive foam
580 reticulation technique, Biomater Adv 136 (2022) 212766.
581 [49] K. Hayashi, T. Yanagisawa, R. Kishida, K. Ishikawa, Effects of Scaffold Shape on Bone
582 Regeneration: Tiny Shape Differences Affect the Entire System, ACS Nano 16(8) (2022) 11755-
583 11768.
584 [50] K. Hayashi, T. Yanagisawa, M. Shimabukuro, R. Kishida, K. Ishikawa, Granular honeycomb

View Article Online
DOI: 10.1039/D6NR01077F

585 scaffolds composed of carbonate apatite for simultaneous intra- and inter-granular osteogenesis
586 and angiogenesis, Mater Today Bio 14 (2022) 100247.
587 [51] C.W. Hargis, I. Chen, Y. Wang, H. Maraghechi, R.J. Gilliam, P.J.M. Monteiro, Microstructure
588 development of calcium carbonate cement through polymorphic transformations, Cement and
589 Concrete Composites 153 (2024).
590 [52] T.A. Kathyola, E.A. Willneff, C.J. Willis, P.J. Dowding, S.L.M. Schroeder, Reactive CaCO(3)
591 Formation from CO(2) and Methanolic Ca(OH)(2) Dispersions: Transient Methoxide Salts,
592 Carbonate Esters and Sol-Gels, ACS Phys Chem Au 4(5) (2024) 555-567.
593 [53] J. Wei, X. Chen, Y. Xu, L. Shi, M. Zhang, M. Nie, X. Liu, Significance and considerations of
594 establishing standardized critical values for critical size defects in animal models of bone tissue
595 regeneration, Heliyon 10(13) (2024) e33768.
596 [54] T. Zhao, C. Xu, Y. Ma, Y. Zeng, N. Wang, Study on preparation and structure of
597 chrysanthemum‐shaped micron calcium carbonate based on inverse microemulsion, Micro &
598 Nano Letters 15(15) (2020) 1151-1155.
599 [55] S. Shahabi, F. Najafi, A. Majdabadi, T. Hooshmand, M. Haghbin Nazarpak, B. Karimi, S.M.
600 Fatemi, Effect of gamma irradiation on structural and biological properties of a PLGA-PEG-
601 hydroxyapatite composite, ScientificWorldJournal 2014 (2014) 420616.
602 [56] A. Antonakos, E. Liarokapis, T. Leventouri, Micro-Raman and FTIR studies of synthetic and
603 natural apatites, Biomaterials 28(19) (2007) 3043-54.
604 [57] H. Madupalli, B. Pavan, M.M.J. Tecklenburg, Carbonate substitution in the mineral
605 component of bone: Discriminating the structural changes, simultaneously imposed by carbonate
606 in A and B sites of apatite, J Solid State Chem 255 (2017) 27-35.
607 [58] F. Ren, Y. Ding, Y. Leng, Infrared spectroscopic characterization of carbonated apatite: a
608 combined experimental and computational study, J Biomed Mater Res A 102(2) (2014) 496-505.
609 [59] A. Averardi, C. Cola, S.E. Zeltmann, N. Gupta, Effect of particle size distribution on the
610 packing of powder beds: A critical discussion relevant to additive manufacturing, Materials Today
611 Communications 24 (2020).
612 [60] J. Katagiri, S. Nomoto, M. Kusano, M. Watanabe, Particle Size Effect on Powder Packing
613 Properties and Molten Pool Dimensions in Laser Powder Bed Fusion Simulation, Journal of
614 Manufacturing and Materials Processing 8(2) (2024).
615 [61] E.B. L.Niel Plummer, The solubilities of calcite, aragonite and vaterite in CO2-H2O solutions
616 between 0 and 90° C, and an evaluation of the aqueous model for the system CaCO3-CO2-H2O,
617 Geochimica et Cosmochimica Acta 46(6) (1982) 1011-1040.
618 [62] D. Xia, Y. Wang, R. Wu, Q. Zheng, G. Zhang, S. Xu, P. Zhou, The effect of pore size on cell
619 behavior in mesoporous bioglass scaffolds for bone regeneration, Applied Materials Today 29
620 (2022).

View Article Online
DOI: 10.1039/D6NR01077F

621

View Article Online
DOI: 10.1039/D6NR01077F

Data availability statement

The data supporting the findings of this study are available within the article.

Additional data are available from the corresponding author upon reasonable request.